

Overview of novel integrated optical ring resonator bio/chemical sensors

Xudong Fan, Ian M. White, Hongying Zhu, Jonathan D. Suter, and Hesam Oveys

Biological Engineering Department, University of Missouri
1201 E. Rollins Street, 240D Life Sciences Center, Columbia, MO 65211

ABSTRACT

In parallel to a stand-alone microsphere resonator and a planar ring resonator on a wafer, the liquid core optical ring resonator (LCORR) is regarded as the third type of ring resonator that integrates microfluidics with state-of-the-art photonics. The LCORR employs a micro-sized glass capillary with a wall thickness of a few microns. The circular cross section of the capillary forms a ring resonator that supports the whispering gallery modes (WGMs), which has the evanescent field in the core, allowing for repetitive interaction with the analytes carried inside the capillary. Despite the small physical size of the LCORR and sub-nanoliter sensing volume, the effective interaction length can exceed 10 cm due to high Q-factor (10^6), significantly improving the LCORR detection limit. The LCORR is a versatile system that exhibits excellent fluid handling capability inherent to capillaries and permits non-invasive and quantitative measurement at any location along the capillary. Furthermore, the LCORR uses the refractive index change as a transduction signal, which enables label-free detection. Therefore, the LCORR is a promising technology platform for future sensitive, miniaturized, lab-on-a-chip type sensors. In this paper, we will introduce the concept of the LCORR and present the theoretical analysis and the experimental results related to the LCORR sensor development.

Keywords: whispering gallery modes, ring resonators, optical sensors, microfluidics, capillary electrophoresis, lab-on-a-chip, label-free detection, refractive index

1. INTRODUCTION

1.1. Optical ring resonator biochemical sensors

Optical microring resonators are an emerging bio/chemical sensing technology that have recently been under intensive investigation.¹⁻³⁷ Ring resonator sensing is similar to conventional straight waveguide sensing.³⁸⁻⁴⁰ We will first briefly compare these two technologies and show the advantages of the ring resonators, and then we will introduce the latest technological advancement – the liquid core optical ring resonator (LCORR) that integrates ring resonators with microfluidics. Like waveguide sensors, optical ring resonators are capable of performing label-free,^{1-10,12-16,18,19,21-28,30,32} fluorescence-labeled,^{20,29-33} and Raman based detection.^{11,17} Here we focus on label-free detection protocol, as it avoids the laborious fluorophore labeling procedures and allows for kinetic measurement of molecule interaction.

A generic label-free waveguide sensor is illustrated in Figure 1(A). Biorecognition molecules, such as antibodies, are immobilized onto the surface of the waveguide. The evanescent field of the guided light in the waveguide extends into the surrounding medium (*e.g.*, water) for approximately 100 nm and interacts with the biomolecules near the waveguide surface. A small change in refractive index near the waveguide surface when target analytes are captured causes modifications in the optical signal (such as phase) at the output, which acts as the sensing signal. Since the sensing signal is accumulative in nature, a longer light-analyte interaction length results in a lower detection limit. In a waveguide sensor, however, the light passes the waveguide only once; consequently, a long (> 1 cm) waveguide may be needed to detect trace quantities of biomolecules, significantly reducing the sensor multiplexing capability and increasing the sample volume.³⁸⁻⁴⁰

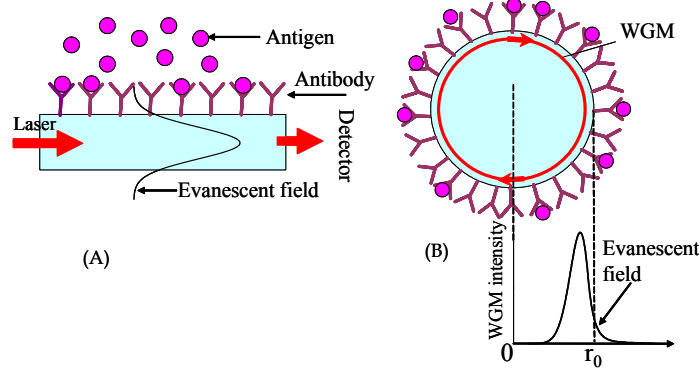


Figure 1: (A) An optical biosensor based on a straight waveguide. (B) An optical ring resonator in which the WGM circulates along its surface.

In contrast, in an optical ring resonator, the light propagates in the form of whispering gallery modes (WGMs),⁴¹⁻⁴³ which result from the total internal reflection of the light along the curved surface. The WGM is a surface mode, and it circulates along the resonator surface and interacts repeatedly with the analytes on its surface through the WGM evanescent field, as illustrated in Figure 1(B). As compared to a straight waveguide sensor, the effective light-analyte interaction length of a ring resonator sensor is no longer determined by the sensor's physical size, but rather by the number of revolutions of the light supported by the resonator, which is characterized by the resonator quality factor, or the Q-factor. The effective length L_{eff} is related to the Q-factor by:^{41,44}

$$L_{eff} = \frac{Q\lambda}{2\pi n}, \quad (1)$$

where λ is wavelength and n is the refractive index of the ring resonator. For example, for a ring resonator with a Q-factor of 10^6 , $n = 1.45$, and $\lambda = 980$ nm, L_{eff} can be as long as 10 cm. Consequently, despite the small physical size of a resonator (50 – 200 μm in diameter), a ring resonator can deliver sensing performance superior to a waveguide while using orders of magnitude less surface area and sample volume. Furthermore, due to the small size of ring resonators, high density sensor integration becomes possible.

Similar to an optical waveguide, the ring resonator utilizes the refractive index change to perform detection. The WGM spectral position, *i.e.*, resonant wavelength, λ , is related to the refractive index through the resonant condition:⁴¹

$$\lambda = \frac{2\pi r n_{eff}}{m}, \quad (2)$$

where r is the ring outer radius, n_{eff} is the effective refractive index experienced by the WGM, and m is an integer that describes the WGM angular momentum. Eq. (2) shows that resonance occurs for wavelengths when an integer multiple of that wavelength matches the circumference. n_{eff} changes when the RI near the ring resonator surface is modified due to the capture of target molecules on the surface, which in turn leads to a shift in the WGM spectral position, as illustrated in Figure 2. Thus, by directly or indirectly monitoring the WGM spectral shift, it is possible to obtain both quantitative and kinetic information about the binding of molecules near the surface. This label-free sensing mechanism allows for

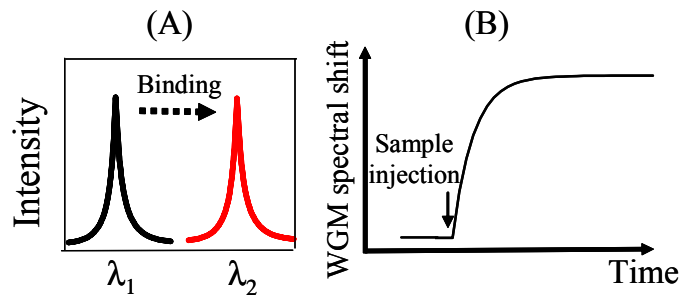


Figure 2: (A) WGM shifts from λ_1 to λ_2 in response to the binding of the target molecules to the LCORR interior surface. (B) Sensorgram is obtained by recording the WGM spectral position as a function of time.

the detection of biomolecules in their natural form without the laborious fluorescent labeling process, as well as the detection of non-fluorescent chemical molecules.

Optical ring resonator sensors have been implemented in two configurations: dielectric discrete microspheres (including its variations such as microtoroids)¹⁻²¹ and planar rings formed on a substrate.²²⁻³⁷ The Q-factor in excess of 10^6 and approximately 10^4 have been achieved for microspheres and planar rings immersed in water, respectively.^{2,12,21,24,26} The sensitivity of 30 nm/RIU (refractive index units) and 140 nm/RIU has been achieved for microspheres and planar rings, leading to a detection limit of 10^{-7} RIU and 10^{-5} RIU.^{4,12,26} It is also shown that the detection limit for biomolecules deposited on the sensor surface can be as low as 1-10 pg/mm².^{2,5,14} Recently, it was demonstrated that the microsphere based ring resonator can ultimately detect small molecules down to the subfemtomole level.¹³ Therefore, the optical microring resonator is a competitive sensing technology that rivals that based on surface plasmon resonance (SPR) based label-free sensors.^{38,45}

An ideal optical ring resonator sensor not only requires high sensitivity and low detection limit, but also needs effective integration at both the photonics level and the fluidics level, which are responsible for delivering light and fluidic samples to the sensing head, respectively. Successful photonics and fluidics incorporation should enable sensor miniaturization, facilitate automated and multiplexed detection, and minimize the sample volume, as has been demonstrated in lab-on-a-chip or micro total analysis system design.⁴⁶⁻⁴⁹ Meanwhile, such incorporation should also help improve detection limit through the techniques such as noise reduction and sample pre-treatment.

While microsphere based sensors exhibit high Q-factor and low detection limit, fluidic integration, mass production, and reproducibility of a microsphere are extremely difficult. On the other hand, planar ring resonators can be mass-produced relatively easily through lithographic or imprint technologies, but they suffer from relatively low Q-factor (10^4 in water²⁴⁻²⁶), which may adversely impact their sensing performance. Furthermore, incorporation of fluidics is non-trivial. Generally, the fluidics needs to be fabricated separately and then mounted onto ring resonator sensors through multiple steps, which may present tremendous design challenges.

1.2. Liquid core optical ring resonator (LCORR) biochemical sensors

In this article, we introduce a novel ring resonator sensing platform centered upon the “liquid core optical ring resonator” (LCORR) that integrates the state-of-the-art photonics with microfluidics.⁵⁰⁻⁵⁷ The concept of the LCORR is illustrated in Figure 3. The LCORR employs a micro-sized glass capillary whose circular cross section forms ring resonators, as illustrated in Figure 3(A). The sample is passed through the LCORR capillary while waveguides arranged perpendicularly to the capillaries deliver light, which couples into the LCORR wall evanescently. The LCORR relies on the presence of the evanescent field of the WGM *in the core* to interact with the sample passing through the capillary, as detailed in Figure 3(B). The LCORR architecture achieves dual use of the capillary as a sensor head and as a fluidic channel. Therefore, the LCORR retains the meritorious high sensitivity and small sample volume of ring resonators while exhibiting the excellent fluid handling capability inherent to capillaries.⁵⁸

As shown in Figure 3, the LCORR design is scalable to a 2-dimensional array for high throughput detection with each capillary being patterned with different biorecognition molecules.⁵⁹⁻⁶¹ It is estimated that ideally 10^3 to 10^4 sensor heads (ring resonators) can be packed onto a 1 cm² chip. This arrangement enables multi-analyte detection and

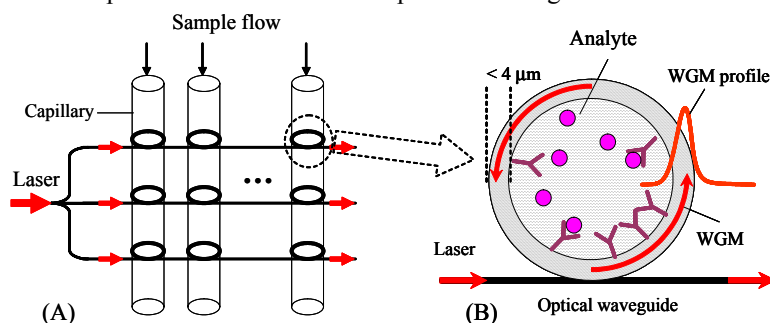
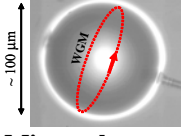
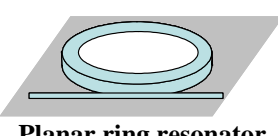
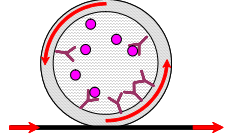


Figure 3: Conceptual illustration of the LCORR sensor array. (A) Top view. Each ring resonator can be immobilized with different biorecognition molecules for multiple-analyte detection. (B) Cross section view. The detection light (WGM) circulates along the ring resonator, monitors the inner surface of the capillary, and reports in real time the binding of target analytes.

minimizes false positives by building in redundancies. Furthermore, for a 1 cm long, 50 μm diameter LCORR, the total sample volume is only 20 nano-liters, with an average of 200 pico-liters (pL) for each ring on the LCORR, assuming that each ring is 100 μm apart along the LCORR.

Like other ring resonator sensors, the LCORR is capable of performing label-free measurements. The binding of biomolecules to the LCORR interior surface or the bulk solution change results in a modification in the effective refractive index experienced by the WGM, leading to a change in the WGM spectral position, as indicated in Eq. (2). In Table 1, we compare the three ring resonator sensing technologies. The details of the LCORR will be elaborated in the following sections.

Table 1: Performance comparison among three ring resonator technologies

	 Microsphere	 Planar ring resonator	 LCORR
Sensitivity	26 nm/RIU ¹²	140 nm/RIU ²⁶	> 30 nm/RIU ⁵²
Q-factor (in water)	$\sim 5 \times 10^6$ ¹²	$\sim 1.2 \times 10^4$ ²⁶	$\sim 1 \times 10^6$ ^{52,55}
Bulk Refractive index change detection limit	3×10^{-7} RIU ¹²	1.8×10^{-5} RIU ²⁶	10^{-6} RIU ^{52,55,56}
Protein detection limit (pg/mm ²)	1-10 ^{2,5,14}	250 ²⁴	10^5 ⁵²
Photonics integration	Very challenging	Easy	Easy (under investigation)
Microfluidics integration	Very challenging	Good (needs to be fabricated separately)	Excellent (inherent to capillary)
Mass-production	Very difficult	Excellent	Good – excellent (under investigation)
Multiplexed detection	Very challenging	Excellent	Excellent (under investigation)

Since the introduction of the LCORR in early 2006,⁵⁰ we have investigated various aspects of the LCORR. We have performed systematical analysis on the LCORR sensitivity under various conditions such as wall thickness, size, operating wavelength, polarization, mode number, *etc.* Additionally, we have analyzed the noise in determination of the LCORR detection limit and the WGM propagation in the LCORR in determination of the WGM spread or ring density along the LCORR. On the experimental side, we have successfully fabricated the LCORR and characterized its sensitivity to the bulk refractive index change in the core. Furthermore, we have demonstrated the feasibility of using the LCORR for biomolecule detection. Coupling between the LCORR and the planar waveguide structures and LCORR-based electro-osmotic flow have also been achieved for future photonic and fluidic integration. In the following sections, theoretical analysis of the LCORR will be presented, followed by the experimental investigations.

2. THEORETICAL ANALYSIS

2.1. General formalism

The WGM of the LCORR can fully be described using Mie theory by considering a three-layered radial structure, as shown in Figure 4(A).^{42,50,54} The radial distribution of the WGM electrical field of an LCORR is governed by:

$$E_{m,l}(r) = \begin{cases} AJ_m(k_{m,l}n_1r) & (r \leq r_1) \\ BJ_m(k_{m,l}n_2r) + CH_m^{(1)}(k_{m,l}n_2r) & (r_1 \leq r \leq r_2) \\ DH_m^{(1)}(k_{m,l}n_3r) & (r \geq r_2) \end{cases}, \quad (3)$$

where J_m and $H_m^{(1)}$ are the m th Bessel function and the m th Hankel function of the first kind, respectively. The refractive index of the core, wall, and the surrounding medium is described by n_1 , n_2 , and n_3 . The terms r_1 and r_2 represent the inner and outer radius of the LCORR, respectively, and $k_{m,l}$ is the amplitude of the wave vector in vacuum for the l th order radial WGM. The resonant wavelength $\lambda_{m,l} = \frac{2\pi}{k_{m,l}}$ can be obtained numerically from Eq. (3) by matching the boundary

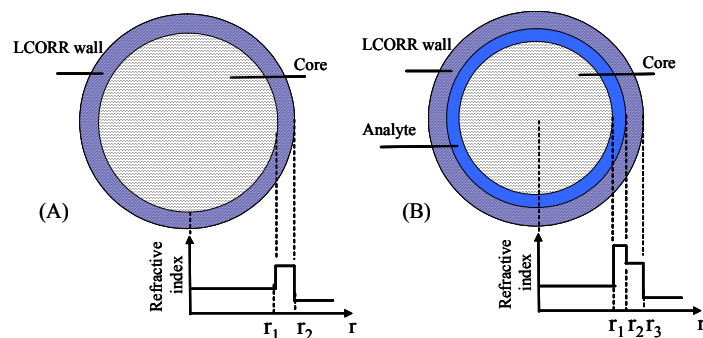


Figure 4: (A) Three-layer model. (B) Four-layer model.

conditions at r_1 and r_2 . The WGM has two polarization states with the electric field being along or perpendicular to the LCORR longitudinal direction. Using this three-layer model, the WGM spectral position can be obtained as a function of wall thickness, the LCORR size, operating wavelength, *etc.*, which allows us to calculate the LCORR sensitivity to bulk refractive index change and to optimize the LCORR design.

For the LCORR with the radius much larger than wavelength, the WGM spectral position can be approximated by Eq. (2), in which n_{eff} is determined by the refractive index of the core (sample), capillary wall, and the surrounding medium (*e.g.*, air).⁵⁴ Eq. (2) significantly simplifies the relationship among the WGM spectral position, refractive index, and the LCORR radius, based on which many theoretical analyses can be performed in a very straightforward and insightful manner.

The three-layer model can further be generalized to include the analyte layer on the inner LCORR wall, as shown in Figure 4(B). In this method, we can use the layer thickness to quantify the amount of biomolecules on the surface and the refractive index to describe different types of biomolecules. This approach would provide a model for the spectral shift due to analyte deposition on the inner surface. Following this, we can determine the shift due to a single analyte molecule, assuming that each molecule is independent and non-interacting, and contributes equally to the spectral shift. Note that this model can easily be extended to include more analyte layers to describe more complicated bio-detection processes.

2.2. Bulk refractive index sensitivity

Label-free optical sensors essentially detect the refractive index change induced by the changes in bulk solution or by the binding of the molecules to the sensor surface. Sensitivity in units of nm/RIU (or, more generally, transduction signal per RIU) provides a measure to characterize the sensor spectral response to the refractive index change, which allows us to compare the performance of sensors based on different types of ring resonators, or even different sensing technologies. Here we use an in-house analysis tool based on Eq. (3) to systematically investigate the LCORR response to bulk refractive index change in the core under various conditions such as wall thickness, operating wavelength, LCORR size, WGM mode number, and WGM polarization.

Sensitivity of the LCORR will depend highly on the LCORR wall thickness. A thinner wall results in a larger evanescent field, which enables higher light-matter interaction, and thus higher sensitivity. This phenomenon is illustrated in Figure 5, in which the light intensity distribution for an LCORR with 2 and 3 μm wall thickness is plotted using Eq. (3) and clearly shows that an LCORR with a 2 μm wall has a higher evanescent field in the core. The sensitivity impact of the wall thickness is presented in Figure 6. The sensitivity for a 3 μm wall is only 3 nm/RIU, while for a 2 μm wall, the sensitivity is as high as 32 nm/RIU. For comparison, the sensitivity for the planar ring resonator of 120 μm in diameter and the 2nd order radial mode ($l = 2$) in a 100 μm diameter microsphere is approximately 140 nm/RIU and 30 nm/RIU, respectively, where in the microsphere case only the outer surface is used for sensing and in the planar ring resonator case the inner, outer, and top surfaces are all utilized for sensing.^{12,26}

For a given geometry of the LCORR, sensitivity is also determined by the operating wavelength. Figure 6 compares the sensitivity when the operating wavelength is increased from 980 nm to 1550 nm, and shows significant increase in sensitivity at 1550 nm, as compared to 980 nm. This is related to the deeper penetration depth of the evanescent field when the wavelength becomes longer. For example, for the same 3 μm wall, the sensitivity is 46 nm/RIU at 1550 nm,

whereas it is only 3 nm/RIU at 980 nm. When the wall thickness becomes 2.3 μm (not shown in Figure 6), the sensitivity is approximately 150 nm/RIU, which is nearly the same as the sensitivity obtained in a planar ring resonator with the similar diameter (120 μm) and the same operating wavelength. The WGM polarization also has an effect on sensitivity. For example, the 2nd order WGM with a wall thickness of 3.5 μm has a sensitivity of 19 nm/RIU at 1550 nm when the polarization is along the LCORR axis (see Figure 6) in comparison with 23.5 nm/RIU sensitivity for the same LCORR

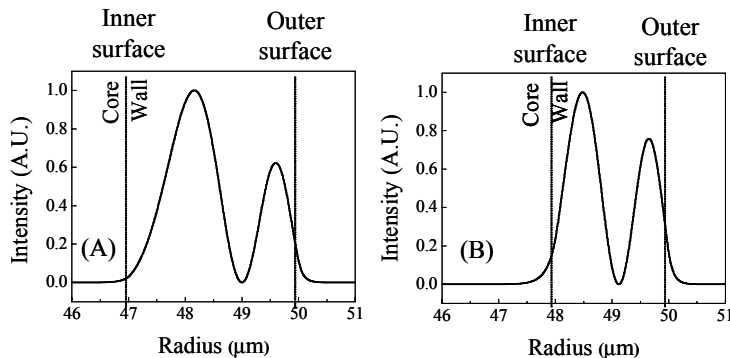


Figure 5: Intensity distribution of the WGMs ($m = 442, l = 2$). Wall thickness = 3 μm (A) and 2.0 μm (B). OD = 100 μm . Refractive index: $n_1 = 1.33, n_2 = 1.45, n_3 = 1.0$. $\lambda \sim 980$ nm. Polarization is along the LCORR longitudinal direction.

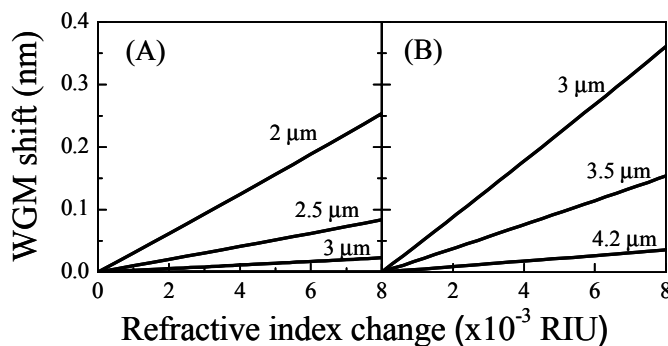


Figure 6: WGM response to the refractive index change in the core for varying wall thicknesses at 980 nm (A) and 1550 nm (B). The slope represents the LCORR refractive index sensitivity. Refractive index: $n_1 = 1.33, n_2 = 1.45, n_3 = 1.0$. Polarization is along the LCORR longitudinal direction. OD = 100 μm .

when the polarization perpendicular to the LCORR axis.

Sensitivity is further dependent upon the radial mode order. The higher order radial mode has a higher evanescent field in the core of the LCORR, resulting in higher light-matter interaction. Figure 7 shows a 2nd and 4th radial mode for the same LCORR. Calculations reveal that the 4th order mode has a sensitivity of 60 nm/RIU, compared to the 3 nm/RIU of the 2nd order mode. Note that this trend is consistent with the conventional ring resonators where higher order modes have more evanescent field available for sensing.^{4,12,20} However, one trade-off of the high sensitivity is that the high amount of light intensity in the core results in a Q-factor degradation from light absorption and scattering, which may deteriorate the overall sensing performance.

Finally, the sensitivity is related to the LCORR size. Figure 8(A) shows the sensitivity dependence upon outer diameter while the thickness of the wall is held constant at 4 μm . As the graph shows, the sensitivity increases with the increased LCORR diameter, in sharp contrast to the conventional ring resonators such as microspheres where the bulk refractive index sensitivity is inversely proportional to the ring size.^{4,12} This phenomenon can be explained by Figure 8(B), which shows the evanescent intensity at the inner surface of the LCORR for diameters of 60 μm and 100 μm . The LCORR with the larger diameter has a stronger evanescent field at the inner surface, thus increasing the light-matter interaction and raising the sensitivity. Another way to account for this is to treat the LCORR as a bent waveguide. Due to bending, the light is redistributed along the radial direction, with more light being outside the LCORR and less inside the core, as compared to the straight waveguide case.⁶² Therefore, a smaller diameter results in a smaller fraction of light in the core, as shown in Figure 9. By the same token, in the limit of infinitely large diameter, the fraction of the light in the

core, and thus the sensitivity, should approach that of a straight waveguide, as shown by the dashed line in Figure 9.

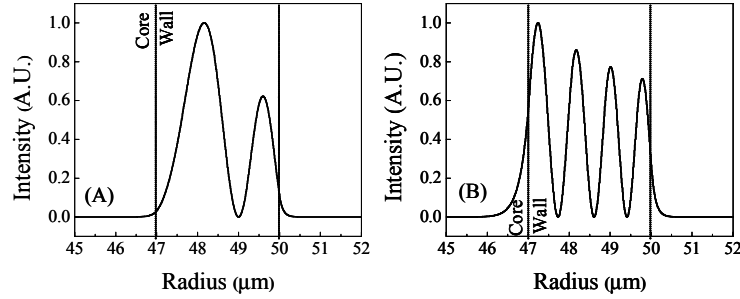


Figure 7: Intensity distribution of the WGMs. (A) $m = 442, l = 2, \lambda = 977.4306$ nm. (B) $m = 415, l = 4, \lambda = 976.7432$ nm. OD = 100 μm. Wall thickness = 3 μm. Refractive index: $n_1 = 1.33, n_2 = 1.45, n_3 = 1.0$.

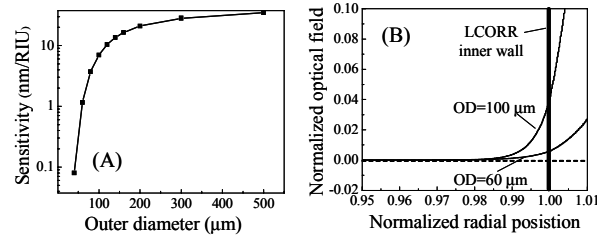


Figure 8: (A) Calculated LCORR sensitivity dependence on the diameter for the 2nd order WGM; the wall thickness is kept constant at 4 μm. (B) Comparison of the evanescent intensities at the interior surface for LCORRs with diameters of 60 μm and 100 μm. Refractive index: $n_1 = 1.33, n_2 = 1.45, n_3 = 1.0$. $\lambda \sim 1550$ nm. Polarization is along the LCORR longitudinal direction.

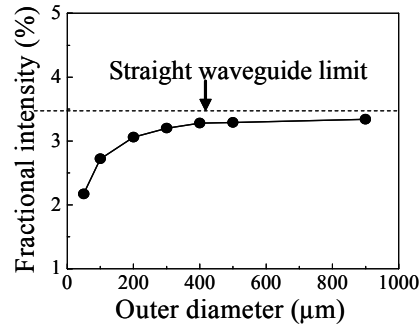


Figure 9: Fraction of the 4th order WGM in the core as a function of the LCORR diameter. Dashed line shows the value in the limit of straight slab waveguide of 2 μm in width. Refractive index: $n_1 = 1.33, n_2 = 1.45, n_3 = 1.0$. $\lambda \sim 980$ nm. Wall thickness: 2 μm. Polarization is along the LCORR longitudinal direction.

2.3. Temperature induced noise

Temperature has significant impact on the performance of label-free optical sensors. For an LCORR, it is critical to precisely determine its WGM spectral position, as it is directly related to the LCORR detection limit. However, the temperature fluctuations deteriorate the LCORR sensing capability by adding noise to the WGM spectral position.⁵⁴ Recalling Eq. (2), we have

$$\frac{\Delta\lambda}{\lambda} = \frac{\partial r}{\partial T} \cdot \frac{1}{r} \Delta T + \frac{\partial n_{eff}}{\partial T} \cdot \frac{1}{n_{eff}} \Delta T, \quad (5)$$

where T is temperature of the LCORR. Eq. (5) can be rewritten in a more explicit form:

$$\frac{\Delta\lambda}{\lambda} = \alpha\Delta T + \frac{\partial n_{eff}}{\partial n_{wall}} \frac{\kappa_{wall}}{n_{eff}} \Delta T + \frac{\partial n_{eff}}{\partial n_{core}} \frac{\kappa_{core}}{n_{eff}} \Delta T, \quad (6)$$

where $\alpha = 1/r \partial r/\partial T$ is the LCORR thermal expansion coefficient and $\kappa_{wall(core)} = \partial n/\partial T$ is the thermo-optic coefficient for the LCORR wall (core). The first term on the right side of Eq. (6) is the noise due to thermal expansion, and the second and the third term represent the respective noise induced by temperature induced refractive index change in the wall and core. For a thick-walled LCORR, the amount of the light in the core is negligible. Therefore, the thermal noise is mainly determined by the first two terms on the right side of Eq. (6), which leads to a temperature dependent WGM shift of approximately 8 pm/K at 1550 nm, as shown in Figure 10. When the LCORR wall becomes thinner, the evanescent field of the WGM in the core, and hence the third term on the right side of Eq. (6), can not be ignored. Since the thermo-optic coefficient for the core, which is typically water (or other organic solutions), is negative and large in magnitude in comparison with that for the wall,^{63,64} the thermal noise is subdued, as demonstrated in Figure 10 with the 3.5 μm thick wall. The simulation in Figure 10 further shows that at certain wall thickness, the water effect will completely counterbalance the thermal noise induced by the wall, leading to elimination of the thermal noise to the first order.

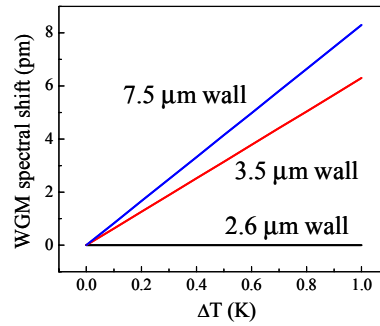


Figure 10: Simulation of the WGM spectral response to temperature change. The LCORR is made of fused silica and filled with water. OD = 100 μm ; $\alpha(\text{wall}) = 5 \times 10^{-7} \text{ K}^{-1}$; $\kappa(\text{wall}) = 6.4 \times 10^{-6} \text{ K}^{-1}$; $\kappa(\text{core}) = -1 \times 10^{-4} \text{ K}^{-1}$. Refractive index: $n_1 = 1.33$; $n_2 = 1.45$; $n_3 = 1$. Wavelength: 1550 nm. Wall thickness is labeled on the figure. Zero thermal sensitivity is achieved when the LCORR wall thickness is 2.6 μm . Polarization is along the LCORR longitudinal direction.

2.4. Pressure induced noise

The WGM spectral position of an LCORR may potentially be susceptible to the variation in the differential pressure between the liquid in the core and the surrounding medium (*e.g.*, atmosphere), as illustrated in Figure 11. The pressure induced WGM change can be expressed as:

$$\frac{\Delta\lambda}{\lambda} = \frac{\Delta r}{r} = \frac{r}{t} \cdot \frac{\Delta P}{E}, \quad (7)$$

where E is the LCORR Young's modulus. For fused silica used in LCORRs, $E = 7 \times 10^{10} \text{ Pa}$. For an LCORR with $r = 100 \mu\text{m}$ and $t = 2 \mu\text{m}$, Eq. (7) becomes:

$$\frac{\Delta\lambda}{\lambda} \approx 10^{-9} \Delta P (\text{Pa}). \quad (8)$$

Generally, the Q-factor for an LCORR is on the order of 10^6 . In order to keep the pressure induced noise small in comparison with the spectral resolution set by the WGM spectral linewidth (or the Q-factor), restrictions on the external pressure that pushes the liquid sample through the LCORR and on the flow rate may need to be imposed, especially when mechanical pumps such as peristaltic pumps are used. For example, if the Q-factor is 10^6 and if we assume that the spectral resolution is one hundredth of the WGM spectral linewidth, then the variation in differential pressure should be kept below 10 Pa.

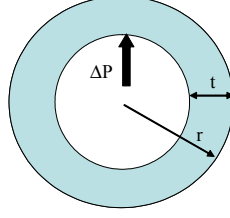


Figure 11: LCORR radius, r , changes under differential pressure (ΔP). t : LCORR thickness.

2.5. Mode extension

The WGM extension along the LCORR axis is important in determining the separation needed between two adjacent ring resonators on the LCORR to avoid any overlap of their respective modes. Unlike microspheres or planar ring resonators on a substrate, in which the curved surface or top/bottom edges defines the mode extension, the LCORR has no confinement along its longitudinal axis (z -direction). Therefore, intuitively, the WGM would spread along this direction indefinitely. It is not the case, however, in a cylindrical ring resonator. In fact, the propagation of the light in an LCORR (or, more generally, a cylindrical ring resonator) can be described using a longitudinal phased array,^{65,66} as illustrated in Figure 12(A), where each element in the array is driven by the external source through the coupling waveguide and emits the coherent light with the fixed phase. Assuming that $E(z,x)$ is the electric field distribution along the LCORR axis (z -direction) at a distance of x away from the waveguide coupling point where the light is fed into the resonator, we have:

$$E(z, x) = \sum_{J=0}^{\infty} \gamma^J e(z, x - J \cdot L), \quad (9)$$

where $L=2\pi r$ is the round trip distance, where r is the ring resonator radius. γ describes the electric field attenuation in one round trip and is related to the Q-factor through $Q = 2\pi n/\alpha\lambda$, where $\alpha = (1-\gamma^2)/L$. e describes the propagation of the electric field of each individual element in the array, and can be approximated by a Gaussian beam:⁶⁷

$$e(z, x) = \frac{w_0}{w(x)} \exp\left(-\frac{z^2}{w^2(x)}\right) \exp\left[-jkx - jk \frac{z^2}{2R(x)} + j \arctan\left(\frac{x}{x_0}\right)\right], \quad (10)$$

where w_0 is the half-width of the Gaussian beam. $w(x) = w_0[1+(x/x_0)^2]^{0.5}$, $x_0 = \pi w_0^2/\lambda$, $R(x) = x+x_0/x$. $k=2\pi n/\lambda$, λ is wavelength in vacuum, and n is the refractive index of the LCORR. Figure 12(B) shows the light intensity distribution at three different locations along the ring resonator circumference. It can be seen that most of the light is confined to within a 100 μm segment along the longitudinal direction of the cylinder due to the interference among the light from the consecutive input through the waveguide.

These results obtained here are of significance in a number of LCORR applications. For example, based on Figure 12(B), we know that the LCORR spatial resolution along its axis is on the order of 10 μm , which is important in LCORR capillary electrophoresis and chromatography for high resolution on-column detection.⁵⁵ Additionally, the sample

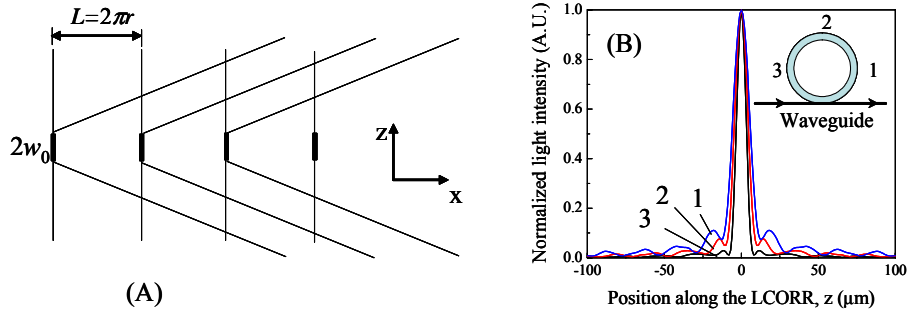


Figure 12: (A) Longitudinal phased array used to simulate the propagation of the WGM in an LCORR. (B) Normalized light intensity distribution along z -direction (LCORR axis direction). Curve 1, 2, and 3 are taken at three different locations along the LCORR circumference. $w_0 = 5 \mu\text{m}$, $\lambda = 980 \text{ nm}$, $n = 1.45$, $r = 50 \mu\text{m}$, $Q = 10^6$. Fraction of light between $-50 \mu\text{m}$ and $50 \mu\text{m}$ is 94%, 92.5%, and 90% for curve 1, 2, and 3, respectively.

detection volume on the order of 100 pL can also be deduced. Finally, the cross-talk between the adjacent ring resonators can be significantly reduced, if the separation of these resonators is larger than 100 μm .

3. EXPERIMENTAL INVESTIGATIONS

3.1. LCORR fabrication

The LCORRs are fabricated by rapidly pulling a glass tube while heating the center section, as illustrated in Figure 13(A). The heat can be provided by a heating coil, a flame, or a CO₂ laser. The foundation of capillary pulling is mass conservation, *i.e.*,⁶⁸

$$\pi[R_0^2 - (R_0 - t_0)^2]V_f = \pi[R_1^2 - (R_1 - t_1)^2]V_p, \quad (11)$$

where R_0 , t_0 , and V_f are the original outer radius, wall thickness, and feed-in speed, respectively. R_1 , t_1 , and V_p are the final outer radius, wall thickness, and pulling speed, respectively. If we assume that there is no surface tension induced capillary collapse involved, the capillary aspect ratio, *i.e.*, $\eta = R/t$ should remain constant. Therefore, by controlling the ratio between the feed-in and pulling speeds, we are able to control the final size of the LCORR and its wall thickness.

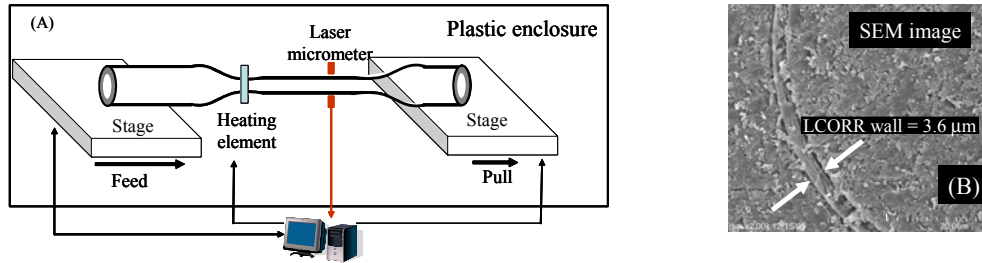


Figure 13: (A) Schematic of LCORR pulling station. (B) SEM image of a portion of the LCORR cross section with OD = 100 μm . Note that to take the image, the LCORR is broken at the sensing region, mounted in UV curable glue, and then polished.

In practice, a certain degree of collapsing may occur due to glass surface tension, as reported in the literature on capillary pulling,⁶⁸⁻⁷¹ leading to a thicker wall, *i.e.*, a lower η value than the initial value. The collapsing effect can be mitigated by using a higher pulling speed and/or lower heating temperature. After systematic investigation in pulling parameters, and quality check of the final size and the wall thickness using an optical microscope, we found that the original η can well be maintained after pulling. In fact, over 95% of the original η was reported in a previous study.⁶⁸

In our experiment, we start with a glass tube with OD = 1.2 mm, ID = 0.9 mm, and $\eta = 4$. To increase η , we pre-etch the glass tubes from outside to reduce the wall thickness by placing them in a hydrofluoric acid (HF) bath. Although pre-etching takes nearly 1.5 hours, tens of glass tubes can be batch-processed simultaneously and stored for later use. After pre-etching, the wall thickness can be reduced down to 75 μm , hence $\eta = 7$. After pulling, the LCORR OD becomes 100 μm , and wall thickness is approximately 7-8 μm .

To further reduce the wall thickness to below 4 μm , a diluted concentration of HF (<1%) is pumped through the LCORR to slightly etch the LCORR interior wall. This etching process, as detailed in Ref. (15, 50), is well controlled and takes approximately 20-60 minutes. When the desired wall thickness is reached, pure water is pumped through the LCORR to terminate the etching process. An SEM image of the final LCORR is shown in Figure 13(B).

One apparent concern of fabricating LCORRs with such a high aspect ratio is mechanical robustness. However, high aspect ratio capillaries have been fabricated previously with no reported mechanical fragility.⁷² Furthermore, we have conducted a number of experiments with LCORRs that have wall thickness of around 2-4 μm . All the LCORRs have demonstrated high mechanical integrity and can even sustain high pressure when fluid is conducted via a mechanical pump.

Further improvement can be made on our current setup. First, it is highly desirable to directly obtain a wall thickness of 2-4 μm without time-consuming HF post-etching, which may also degrade the Q-factor due to the surface roughness introduced during the etching process. To achieve further reduction in the wall thickness to the preform, more HF pre-

etching may be needed. Second, while our current setup can produce LCORRs of fairly uniform size, a laser micrometer can be implemented, as shown in Figure 13(A), to characterize the LCORR size *in-situ* and in real-time, which will provide feedback for a better quality control in LCORR fabrication. It is expected that our system will produce LCORRs of tens of centimeters in length with uniform quality, which can further be diced into shorter pieces for sensor arrays.

3.2. Experimental setup

The setup for LCORR sensor characterization is illustrated in Figure 14. The sample is driven into the LCORR with a peristaltic pump. Light from a tunable laser diode (external cavity laser from New Focus or DFB laser from JDSU) is coupled into the WGM through the evanescent coupling by an optical fiber taper or a waveguide in contact with the LCORR exterior surface. The tunable laser periodically scans across a wavelength range of about 100 pm while Detector #1 at the output of the waveguide or fiber taper measures the optical power. As shown in Figure 13(D), when the laser wavelength matches the WGM resonant condition, the light couples into the ring resonator and causes the measured transmission power to drop, leaving a spectral dip at Detector #1. In the meantime, the light coupled into the LCORR is scattered off the LCORR surface and can be detected as a spectral peak with a detector placed above the LCORR (Detector #2). Both of the measured signals can be used to indicate the WGM spectral position. The first scheme (Detector #1) is easy to implement and the second scheme (Detector #2) is more suitable when multiple LCORRs are used for high-throughput analysis. The WGM shifts in response to the refractive index change near the LCORR interior surface resulting from the capture of target molecules on the inner LCORR surface. A data acquisition card is used in conjunction with a computer to record the signal from the detector. The sensorgram can subsequently be obtained when the WGM position is plotted as a function of time, as shown in Figure 2. The advantage of this approach is that it is direct and simple to implement. It has a large dynamic range (limited only by the laser scanning range) and signal linearity. Additionally, it can handle multiple ring resonator sensors, as each ring resonator may not have exactly the same WGM position. The drawback is the data acquisition rate, as a large set of data needs to be acquired and saved. In our experiment, up to 10 Hz of scanning rate is used. Although the current scanning rate may go even higher, it is adequate for most of applications in bio/chemical sensing.

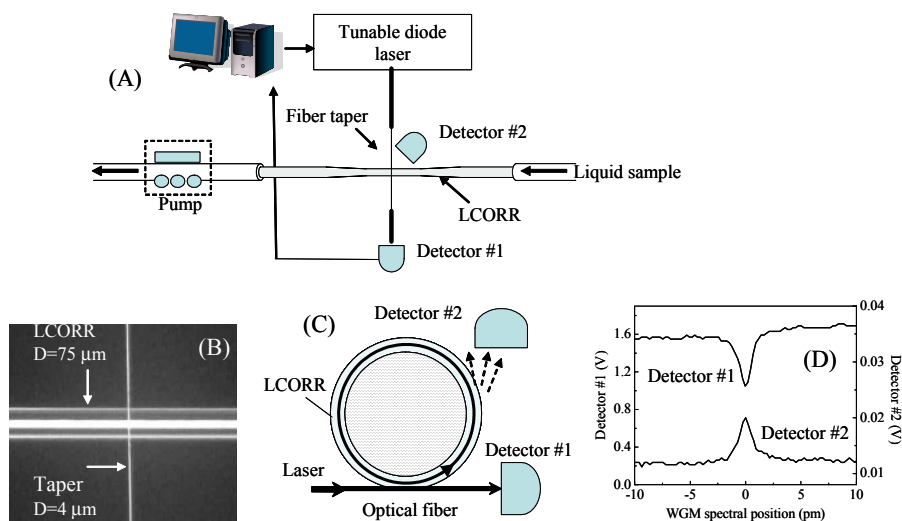


Figure 14: (A) Experimental setup. (B) A picture of the LCORR in touch with an optical fiber taper. (C) Details of the WGM detection. (D) Signals from Detector #1 and #2 to indicate the WGM spectral position.

An alternative and indirect approach, as illustrated in Figure 15, can also be exploited by fixing the laser spectral position to match half of the peak WGM intensity, and then monitoring the laser transmission intensity.^{24,26} A similar detection scheme has also been employed in surface plasmon resonance imaging.⁷³ The advantage is the data acquisition speed. The main disadvantage includes low dynamic range and susceptibility to laser intensity fluctuation. Furthermore, it may not be suitable to handle multiple rings when the WGM of each resonator is not at the same spectral location.

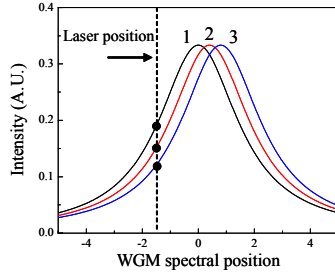


Figure 15: The laser transmission intensity is used to monitor the WGM spectral

3.3. Bulk refractive index characterization

To characterize the LCORR response to the bulk refractive index change, various concentrations of ethanol-water mixture with well-characterized refractive index are passed through the LCORR,^{12,74} while the WGM is monitored. Figure 16(A) shows the sensorgram when the ethanol-water mixture is pumped through the LCORR initially filled with water ($n=1.33$), followed by the rinsing with pure water. A sensitivity of 20 nm/RIU can be calculated when the WGM shift is plotted against the refractive index change. In Ref. (52), we have achieved a sensitivity in excess of 30 nm/RIU, on par with that obtained in a microsphere of the similar diameter.

The refractive index detection limit (DL) can be estimated by:

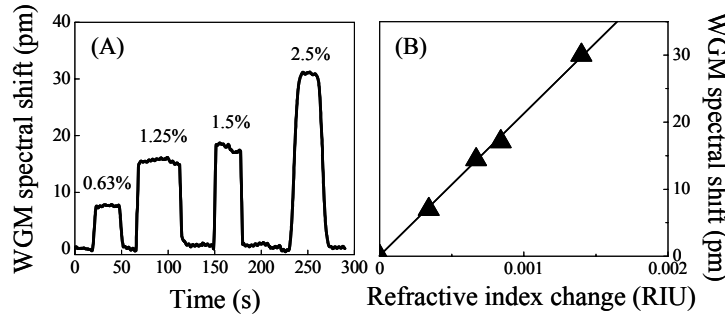


Figure 16: (A) Sensorgram of the WGM response to various concentrations of ethanol. Ethanol concentrations (v/v) are labeled in the figure. (B) LCORR sensitivity curve obtained with a linear fit of the data. Wavelength = 980 nm.

$$DL = \delta / S \quad (12)$$

where δ is the system spectral resolution in units of pm, which determines the system spectral resolution. S is the LCORR sensitivity in units of nm/RIU. δ is mainly determined by two factors, *i.e.*, the LCORR thermal noise and the WGM spectral linewidth. As discussed previously, the LCORR is inevitably influenced by the temperature fluctuations, as nearly all other refractive index sensors. In Figure 17(A), we experimentally characterize the LCORR response to the temperature and show that the WGM of the thin-walled LCORR (4 μm wall thickness) drifts at a rate of approximately 5 pm/K. This rate is lower than that for the thick-walled LCORR due to the water effects, as discussed in Section 2.3. A thinner wall will lead to an even smaller thermal drift rate. To stabilize the temperature, the LCORR is placed on the top of a thermo-electric cooler with a thermistor feedback loop, both of which are connected to a temperature controller (ILX Lightwave 5910). Figure 17(B) shows that the standard deviation of the thermal noise, σ , is 0.0048 pm, which results in a spectral resolution better than 0.02 pm (3σ).

The Q-factor of the LCORR ranges from 5×10^5 to 2×10^6 , and is mainly limited by the roughness on the LCORR inner surface due to HF etching. Assuming that $Q = 10^6$ and that we are capable of detecting a spectral change of one fiftieth of the WGM linewidth,³ we arrive at the spectral resolution of 0.02 and 0.03 pm for 980 nm and 1550 nm, respectively. As a result, δ can conservatively be chosen to be 0.04 pm in Eq. (12). Furthermore, given that $S = 30$ nm/RIU, we can achieve a refractive index detection limit better than 2×10^{-6} RIU in the LCORR.

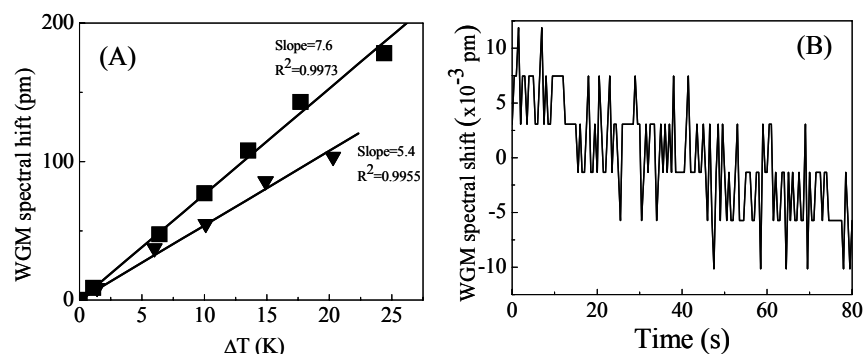


Figure 17: (A) WGM shift in response to temperature change for thick-walled LCORR (square, wall thickness = 8 μm) and thin-walled LCORR (circle, wall thickness = 4 μm). Solid lines are simulation curves based on Eq. (3). (B) LCORR noise with thermo-electric cooler. $\sigma = 0.0048$ pm. Wavelength = 1550 nm. Wavelength scanning step size = 0.004 pm.

It should be noted that although the LCORR sensitivity is nearly five times less than that in planar ring resonators and a few hundred times lower than that demonstrated in SPR based sensors,^{24,26,45} the LCORR has the same or even better refractive index detection limit than the other two types of sensors due to its excellent spectral resolution. In planar ring resonator and SPR sensors, the Q-factor, which is approximately 10^4 and 10, respectively, is the dominant factor that limits the sensor detection limit. In addition, since a significant portion of the light in SPR is in the surrounding medium (water), the temperature induced fluctuation in the water refractive index will ultimately set the detection limit in SPR sensors. Considering that thermo-optic coefficient of water is $-1 \times 10^{-4}/\text{K}$,⁶³ a temperature stability of 0.01 K results in a refractive index detection limit of 10^{-6} RIU. In an LCORR, as shown earlier, water counteracts the temperature induced fluctuations in the WGM spectral position and both the Q-factor and temperature stability play a nearly equal role. Therefore, an excessive increase in the Q-factor may not yield significant improvement in the detection limit.

One method to further lower the detection limit is to implement a reference channel as shown in Figure 18. Common-mode noise such as non-specific binding of molecules and temperature fluctuations can be factored out. Another method is to increase the sensor sensitivity by pushing more light into the core to increase the light-matter interaction. Further reduction in the wall thickness and/or implementation of certain type of photonic structures such as concentric rings^{34,75-77} may be foreseeable in the near future.

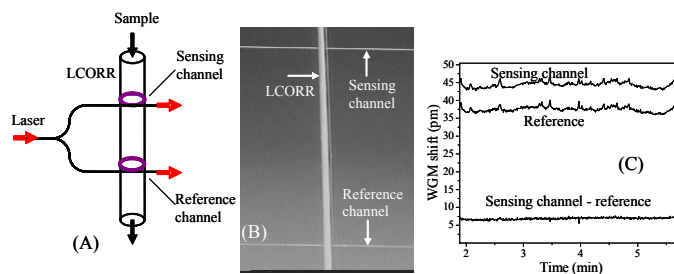


Figure 18: (A) Schematic of an LCORR with a reference channel; (B) A picture of such a setup; (C) Common-mode noise reduction by subtracting the reference from the actual sensing signal.

3.5. Biomolecule detection

Since biomolecules have different refractive indices than buffers that consist mainly of water,^{2,78,79} the WGM shifts when biomolecules attach to the LCORR inner surface in replacement of water molecules. In Figure 19, we demonstrate the detection of bovine serum albumin (BSA) molecules adsorbing to the surface of the LCORR. First, the LCORR inner surface is activated with a 1% (v/v) solution of 3-aminopropyltrimethoxysilane in 10/90 (v/v) water/ethanol. Then a 1 mg/ml solution of BSA in PBS buffer solution was pumped through the LCORR. The resulting sensing signal is plotted in Figure 19. The saturating characteristic of the curve verifies the Langmuir monolayer behavior of the BSA adsorption onto the silane layer. The total WGM spectral shift at the saturation is approximately 41 pm. Assuming that the LCORR surface is fully covered by a monolayer of BSA,^{2,3,14} we can estimate the BSA mass density to be 2.96

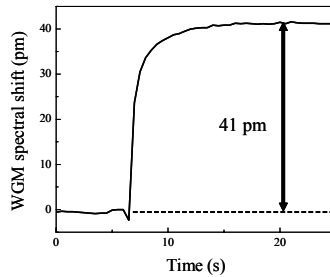


Figure 19: WGM response to BSA adsorption to the LCORR inner surface. Saturation shift = 41 pm.

ng/mm^2 (BSA molecular weight = 66,000 Dalton), which leads to a BSA detection limit less than 10 pg/mm^2 , if we use 0.1 pm as the sensor spectral resolution. The LCORR used here has an OD of approximately $100 \text{ }\mu\text{m}$. Therefore, the 10 pg/mm^2 corresponds to a total of 30 fg molecules, if a mode extension of $10 \text{ }\mu\text{m}$ along the LCORR longitudinal direction is assumed (see Section 2.5). Certainly, this weight detection limit is over estimated due to imperfect surface coverage.

3.6. LCORR based electro-osmotic flow

In addition to sensing, the LCORR exhibits excellent fluidic handling capability inherent to capillaries.⁵⁸ Therefore, a number of technologies developed for capillaries such as sample delivery, pre-concentration, and separation can directly be implemented with the LCORR, which will be extremely useful in device miniaturization and on-chip fluid control and sample processing. In Figure 20, we have demonstrated the feasibility of using an electro-kinetic pump to deliver the fluid samples. Two electrodes are placed in respective reservoirs at each end of the LCORR and the voltage on the electrodes is periodically oscillated (see Figure 20(A)). Figure 20(B) shows the LCORR's sensing response as the analyte repeatedly passes the sensing region of the LCORR. The electric field needed is less than 100 V/cm , which can readily be obtained with a small on-board voltage control in a future miniaturized lab-on-a-chip design.

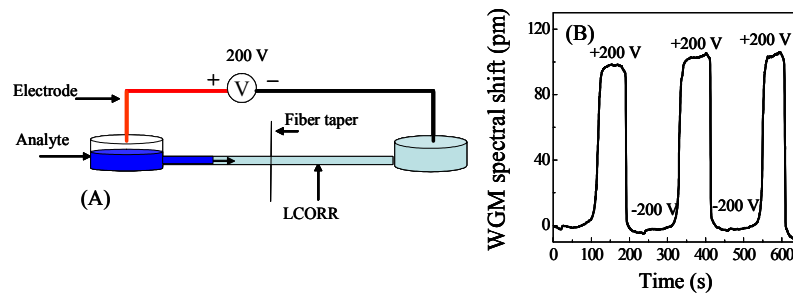


Figure 20: (A) Experimental setup with an electro-osmotic flow system; (B) The WGM shifts when the analyte (glycerol) is driven back and forth through the location of the ring resonator defined by the optical fiber taper.

3.7. Integration with waveguides

Now that we have demonstrated the capability of using an optical fiber taper to couple the resonant light into the LCORR, it is important to fully integrate the LCORR with photonic circuits for future device miniaturization and multiplexing. Optical fiber tapers suffer from low reproducibility, low product yield, and lack of fabrication control. Furthermore, fiber tapers are mechanically fragile. Also it is difficult to position an array of tapers to the desired locations on the LCORR. Lithographically fabricated waveguide arrays on a wafer are advantageous owing to mass production capability, well-controlled fabrication processes, and high channel density. Moreover, they are also highly compatible with opto-electronics, which enables integration with electronics and on-chip lasers in the future.

In our experiment, we use a special type of waveguide, called anti-resonant reflecting optical waveguide (ARROW),⁸⁰⁻⁸⁴ to excite the WGM in an LCORR. An ARROW, as schematically shown in Figure 21, consists of a low refractive index core and a high-low refractive index pair of cladding layers. The thickness of the high index layer has to meet the following condition for the core to guide the light:

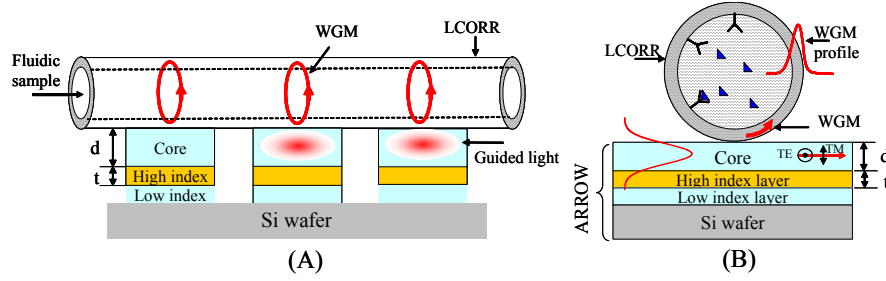


Figure 21: Schematic of the ARROW-LCORN system viewed along the ARROW direction (A) and the LCORN direction (B).

$$t = \frac{\lambda}{4n_2} (2N + 1) \left(1 - \frac{n_1^2}{n_2^2} + \frac{\lambda^2}{4n_2^2 d^2} \right)^{-\frac{1}{2}} \quad (N = 0, 1, 2, \dots), \quad (13)$$

where λ is the laser wavelength in vacuum, n_1 and n_2 are the refractive index of the core and high index layer, respectively, and d is the thickness of the core. Under this anti-resonance condition, the ARROW prevents the light in the core from leaking into the substrate, and in the meantime presents a sufficient evanescent field above the core for the coupling between the ARROW and the LCORN. In an ARROW, only TE-polarized light will propagate whereas the TM-mode is very lossy and can not be transmitted through the ARROW.

Similar to the coupling between the ARROW and a microsphere ring resonator that has previously been achieved,⁸²⁻⁸⁴ the coupling between the ARROW and the LCORN can be accomplished by placing the LCORN in touch with the ARROW channels, as shown in Figure 22. Furthermore, the coupling can be adjusted by changing the ARROW core height.^{51,57} Our results will enable the development of integrated high throughput sensor arrays.

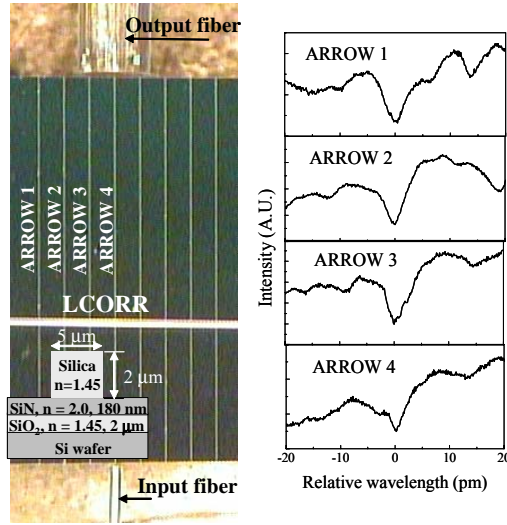


Figure 22: Experimental setup for simultaneous excitation of the WGMs along an LCORN. The inset in the picture shows the detail of the ARROW structure designed to transmit 980 nm light.

3.8. Patterning LCORN inner surface

In order to immobilize multiple biorecognition molecules such as antibody or aptamer on an LCORN, we use a photo-assisted molecular grafting method.⁵⁹⁻⁶¹ As illustrated in Figure 23(A), the inner surface of the LCORN is first silanized with thiol or amine functional groups, then a photo-sensitive cross-linker such as N-5-Azido-2-nitrobenzoyloxysuccinimide in solution is introduced, followed by exposure to a UV lamp or high intensity Argon laser through a photo-mask. Finally, the biorecognition molecule is introduced and immobilized at the exposed locations. Multiple exposures can be repeated to immobilize different types of biorecognition molecules. Figure 23(B) shows the immobilization result obtained with a single window photo-mask exposed to an Argon laser.

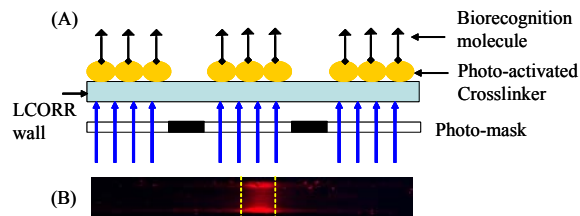


Figure 23: (A) Molecule patterning through photo-assisted molecular grafting. (B) Pattern achieved with a single-window photo-mask. The biorecognition molecules are labeled with fluorescent dye molecules to guide the eye.

4. SUMMARY

In this article, we introduce a novel sensing technology platform based on the LCORR that integrates state-of-the-art photonic sensing performance with excellent fluidic handling capability. We have carried out a series of studies on both theoretical and experimental aspects of the LCORR in order to characterize and understand the LCORR as a sensor. The detection limits for bulk refractive index and protein molecules have been shown to be competitive with the SPR based label-free sensors. This excellent sensing performance, further boosted by the sub-nanoliter detection volume and the potential to scale up for multiplexed detection, will open a door to a broad range of applications in life sciences research, pharmaceuticals, clinics, homeland security, battlefield, and the food industry.

To fully realize the potential of the LCORR, further investigations will be conducted, which are aimed at the following goals:

- (1) Systematic fabrication of the LCORRs;
- (2) Theoretical analysis and modeling of the interaction between a single molecule and the WGM in the LCORR;
- (3) Implementation of photonic crystal structure to further enhance the light-matter interaction, and hence sensitivity;
- (4) Interfacing with the microfluidics;
- (5) Specific applications such as clinical applications (*e.g.*, biomarker detection), small molecule detection for drug discovery, bacterial detection for the food industry, and explosive and toxin detection for defense and homeland security.

These studies, along with those presented in this article, will eventually lead to the commercialization of the LCORR based lab-on-a-chip devices in the future.

In addition to sensing, the LCORR also provides a technology platform for development of novel instruments in analytical chemistry such as capillary electrophoresis and chromatography,⁵⁵ as well as novel opto-fluidic devices such as micro-lasers and reconfigurable filters,⁸⁵⁻⁸⁸ which we will discuss in detail in the future.

ACKNOWLEDGMENTS

The authors acknowledge the financial support from the 3M Non-Tenured Faculty Award, the University of Missouri Research Board Award, the University of Missouri Bioprocessing & Biosensing Center, University of Missouri Research Council, American Chemistry Society Petroleum Research Fund, and Wallace H. Coulter Early Career Award. I. M. White is supported by the MU Life Sciences Fellowship Program and by the NIH Postdoctoral Fellowship. They also thank Dr. Terry L. Smith and Dr. Junying Zhang from 3M Company for ARROW samples and Prof. Michael Raymer from University of Oregon for stimulating discussion on phased array.

REFERENCES

1. A. Serpenguzel, S. Arnold, and G. Griffel, "Excitation of resonances of microspheres on an optical fiber," *Opt. Lett.*, **20**, 654-656, 1995.
2. F. Vollmer, D. Braun, A. Libchaber, M. Khoshima, I. Teraoka, and S. Arnold, "Protein detection by optical shift of a resonant microcavity," *Appl. Phys. Lett.*, **80**, 4057-4059, 2002.
3. S. Arnold, M. Khoshima, I. Teraoka, S. Holler, and F. Vollmer, "Shift of whispering-gallery modes in microspheres by protein adsorption," *Opt. Lett.*, **28**, 272-274, 2003.
4. I. Teraoka, S. Arnold, and F. Vollmer, "Perturbation approach to resonance shifts of whispering-gallery modes in a dielectric microsphere as a probe of a surrounding medium," *J. Opt. Soc. Am. B*, **20**, 1937-1947, 2003.
5. F. Vollmer, S. Arnold, D. Braun, I. Teraoka, and A. Libchaber, "Multiplexed DNA Quantification by Spectroscopic Shift of Two Microsphere Cavities," *Biophys. J.*, **85**, 1974-1979, 2003.
6. M. Noto, M. Khoshima, D. Keng, I. Teraoka, V. Kolchenko, and S. Arnold, "Molecular weight dependence of a whispering gallery mode biosensor," *Appl. Phys. Lett.*, **87**, 223901, 2005.
7. M. Noto, F. Vollmer, D. Keng, I. Teraoka, and S. Arnold, "Nanolayer characterization through wavelength multiplexing of a microsphere resonator," *Opt. Lett.*, **30**, 510-512, 2005.
8. I. Teraoka and S. Arnold, "Theory of resonance shifts in TE and TM whispering gallery modes by nonradial perturbations for sensing applications," *J. Opt. Soc. Am. B*, **23**, 1381-1389, 2006.
9. I. Teraoka and S. Arnold, "Enhancing the sensitivity of a whispering-gallery mode microsphere sensor by a high-refractive-index surface layer," *J. Opt. Soc. Am. B*, **23**, 1434-1441, 2006.
10. X. Fan, P. Palinginis, S. Lacey, H. Wang, and M. C. Lonergan, "Coupling semiconductor nanocrystals to a fused-silica microsphere: a quantum-dot microcavity with extremely high Q factors," *Opt. Lett.*, **25**, 1600-1602, 2000.
11. I. M. White and X. Fan, "Demonstration of composite microsphere cavity and surface enhanced raman spectroscopy for improved sensitivity," *Chemical and Biological Sensors for Industrial and Environmental Security*, Proc. SPIE **5994**, 59940G, 2005.
12. N. M. Hanumegowda, C. J. Stica, B. C. Patel, I. M. White, and X. Fan, "Refractometric sensors based on microsphere resonators," *Appl. Phys. Lett.*, **87**, 201107, 2005.
13. I. M. White, N. M. Hanumegowda, and X. Fan, "Subfemtomole detection of small molecules with microsphere sensors," *Opt. Lett.*, **30**, 3189-3191, 2005.
14. N. M. Hanumegowda, I. M. White, H. Oveys, and X. Fan, "Label-Free Protease Sensors Based on Optical Microsphere Resonators," *Sens. Lett.*, **3**, 315-319, 2005.
15. I. M. White, N. M. Hanumegowda, H. Oveys, and X. Fan, "Tuning whispering gallery modes in optical microspheres with chemical etching," *Opt. Express*, **13**, 10754-10759, 2005.
16. N. M. Hanumegowda, I. M. White, and X. Fan, "Aqueous mercuric ion detection with microsphere optical ring resonator sensors," *Sens. Actuators B*, **120**, 207-212, 2006.
17. I. M. White, H. Oveys, and X. Fan, "Increasing the Enhancement of SERS with Dielectric Microsphere Resonators," *Spectroscopy*, April, 2006.
18. H. Zhu, J. D. Suter, I. M. White, and X. Fan, "Aptamer Based Microsphere Biosensor for Thrombin Detection," *Sensors*, **6**, 785-795, 2006.
19. J. P. Rezac and A. T. Rosenberger, "Locking a microsphere whispering-gallery mode to a laser," *Opt. Express*, **8**, 605 - 610, 2001.
20. J. L. Nadeau, V. S. Ilchenko, D. Kossakovski, G. H. Bearman, and L. Maleki, "High-Q whispering-gallery mode sensor in liquids," *Laser Resonators and Beam Control V*, A. V. Kudryashov, ed., Proc. SPIE **4629**, 172-180, 2002.
21. A. M. Armani and K. J. Vahala, "Heavy water detection using ultra-high-Q microcavities," *Opt. Lett.*, **31**, 1896-1898, 2006.
22. H. Quan and Z. Guo, "Simulation of whispering-gallery-mode resonance shifts for optical miniature biosensors," *Journal of Quantitative Spectroscopy & Radiative Transfer*, **93**, 231-243, 2005.
23. C.-Y. Chao and L. J. Guo, "Biochemical sensors based on polymer microrings with sharp asymmetrical resonance," *Appl. Phys. Lett.*, **83**, 1527-1529, 2003.
24. C.-Y. Chao, W. Fung, and L. J. Guo, "Polymer microring resonators for biochemical sensing applications," *IEEE J. Sel. Top. Quantum Electron.*, **12**, 134-142, 2006.

25. J. Yang and L. J. Guo, "Optical sensors based on active microcavities," *IEEE J. Sel. Top. Quantum Electron.*, **12**, 143-147, 2006.
26. A. Yalcin, K. C. Popat, O. C. Aldridge, T. A. Desai, J. Hryniewicz, N. Chbouki, B. E. Little, O. King, V. Van, S. Chu, D. Gill, M. Anthes-Washburn, M. S. Unlu, and B. B. Goldberg, "Optical Sensing of Biomolecules Using Microring Resonators," *IEEE J. Sel. Top. Quantum Electron.*, **12**, 148-155, 2006.
27. A. Ksendzov and Y. Lin, "Integrated optics ring-resonator sensors for protein detection," *Opt. Lett.*, **30**, 3344-3346, 2005.
28. A. Ksendzov, M. L. Homer, and A. M. Manfreda, "Integrated optics ring-resonator chemical sensor with polymer transduction layer," *Electron. Lett.*, **40**, 2004.
29. E. Krioukov, D. Klunder, A. Driessen, J. Grevea, and C. Otto, "Two-photon fluorescence excitation using an integrated optical microcavity: a promising tool for biosensing of natural chromophores," *Talanta*, **65**, 1086-1090, 2005.
30. E. Krioukov, J. Greve, and C. Otto, "Performance of integrated optical microcavities for refractive index and fluorescence sensing," *Sens. Actuators B*, **90**, 58-67, 2003.
31. E. Krioukov, D. J. W. Klunder, A. Driessen, J. Greve, and C. Otto, "Integrated optical microcavities for enhanced evanescent-wave spectroscopy," *Opt. Lett.*, **27**, 1504-1506, 2002.
32. R. W. Boyd and J. E. Heebner, "Sensitive disk resonator photonic biosensor," *Appl. Opt.*, **40**, 5742-5747, 2001.
33. S. Blair and Y. Chen, "Resonant-enhanced evanescent-wave fluorescence biosensing with cylindrical optical cavities," *Appl. Opt.*, **40**, 570-582, 2001.
34. J. Scheuer, W. M. J. Green, G. A. Derose, and A. Yariv, "InGaAsP Annular Bragg Lasers: Theory, Applications, and Modal Properties," *IEEE J. Quantum Electron.*, **11**, 476-484, 2005.
35. T. Baehr-Jones, M. Hochberg, C. Walker, and A. Scherer, "High-Q ring resonators in thin silicon-on-insulator," *Appl. Phys. Lett.*, **85**, 3346-3347, 2004.
36. T. Baehr-Jones, M. Hochberg, C. Walker, and A. Scherer, "High-Q optical resonators in silicon-on-insulator-based slot waveguides," *Appl. Phys. Lett.*, **86**, 081101, 2005.
37. V. R. Almeida, Q. Xu, C. A. Barrios, and M. Lipson, "Guiding and confining light in void nanostructure," *Opt. Lett.*, **29**, 1209-1211, 2004.
38. R. Narayanaswamy and O. S. Wolfbeis, *Optical Sensors*, Springer, New York, 2004.
39. L. M. Lechuga, A. T. M. Lenferink, R. P. H. Kooyman, and J. Greve, "Feasibility of evanescent wave interferometer immunosensors for pesticide detection: chemical aspects," *Sens. Actuators B*, 762-765, 1995.
40. C. R. Lavers, K. Itoh, S. C. Wu, M. Murabayashi, I. Mauchline, G. Stewart, and T. Stout, "Planar optical waveguides for sensing applications," *Sens. Actuators B*, **69**, 85-95, 2000.
41. R. K. Chang and A. J. Campillo, *Optical Processes in Microcavities*, World Scientific, Singapore, 1996.
42. C. F. Bohren and D. R. Huffman, *Absorption and Scattering of Light by Small Particles*, John Wiley & Sons, New York, 1998.
43. K. Vahala, *Optical Microcavities*, World Scientific, Singapore, 2005.
44. M. L. Gorodetsky, A. A. Savchenkov, and V. S. Ilchenko, "Ultimate Q of optical microsphere resonators," *Opt. Lett.*, **21**, 453-455, 1996.
45. J. Homola, S. S. Yee, and G. Gauglitz, "Surface plasmon resonance sensors: review," *Sens. Actuators B*, **54**, 3-15, 1999.
46. D. R. Reyes, D. Iossifidis, P.-A. Auroux, and A. Manz, "Micro Total Analysis Systems. 1. Introduction, Theory, and Technology," *Anal. Chem.*, **74**, 2623 - 2636, 2002.
47. P.-A. Auroux, D. Iossifidis, D. R. Reyes, and A. Manz, "Micro Total Analysis Systems. 2. Analytical Standard Operations and Applications," *Anal. Chem.*, **74**, 2637 - 2652, 2002.
48. P. S. Dittrich, K. Tachikawa, and A. Manz, "Micro Total Analysis Systems. Latest Advancements and Trends," *Anal. Chem.*, **78**, 3887-3908, 2006.
49. O. Geschke, H. Klank, and P. Telleman, *Microsystem Engineering of Lab-on-a-chip Devices*, John Wiley & Sons, Weinheim, 2004.
50. I. M. White, H. Oveys, and X. Fan, "Liquid Core Optical Ring Resonator Sensors," *Opt. Lett.*, **31**, 1319-1321, 2006.
51. I. M. White, H. Oveys, X. Fan, T. L. Smith, and J. Zhang, "Integrated multiplexed biosensors based on liquid core optical ring resonators and antiresonant reflecting optical waveguides," *Appl. Phys. Lett.*, **89**, 191106-191101 - 191106-191103, 2006.

52. I. M. White, H. Zhu, J. D. Suter, H. Oveys, and X. Fan, "Liquid core optical ring resonator label-free biosensor array for lab-on-a-chip development," *Smart Medical and Biomedical Sensor Technology IV*, Brian M. Cullum and J. Chance Carter, ed., Proc. SPIE **6380**, 63800F, 2006.
53. I. M. White, H. Zhu, H. Oveys, and X. Fan, "Bio/chemical sensors based on liquid core optical ring resonator," *Micro (MEMS) and Nanotechnologies for Space Applications*, Thomas George and Zhong-Yang Cheng, ed., Proc. SPIE **6223**, 62230F, 2006.
54. J. D. Suter, I. M. White, H. Zhu, and X. Fan, "Thermal Characterization of Liquid Core Optical Ring Resonator Sensors," *Appl. Opt.*, in press.
55. H. Zhu, I. M. White, J. D. Suter, M. Zourob, and X. Fan, "An Integrated Refractive Index Optical Ring Resonator Detector for Capillary Electrophoresis," *Anal. Chem.*, in press.
56. I. M. White, H. Zhu, J. D. Suter, N. M. Hanumegowda, H. Oveys, M. Zourob, and X. Fan, "Refractometric Sensors for Lab-on-a-Chip Based on Optical Ring Resonators," *IEEE Sens. J.*, in press.
57. I. M. White, H. Oveys, X. Fan, T. L. Smith, and J. Zhang, "Demonstration of a liquid core optical ring resonator sensor coupled with an ARROW waveguide array," *Integrated Optics: Devices, Materials, and Technologies XI*, Yakov Sidorin and Christoph A. Waechter, ed., Proc. SPIE **6475**, 6475-6403, 2006.
58. J. P. Landers, *Handbook of Capillary Electrophoresis*, CRC Press, 1996.
59. M. Y. Balakirev, S. Porte, M. Vernaz-Gris, M. Berger, J.-P. Arie, B. Fouque, and F. Chatelain, "Photochemical Patterning of Biological Molecules Inside a Glass Capillary," *Anal. Chem.*, **77**, 5474-5479, 2005.
60. F. S. Ligler, M. Breimer, J. P. Golden, D. A. Nivens, J. P. Dodson, T. M. Green, D. P. Haders, and O. A. Sadik, "Integrating Waveguide Biosensor," *Anal. Chem.*, **74**, 713-719, 2002.
61. M. A. Holden, S.-Y. Jung, and P. S. Cremer, "Patterning Enzymes Inside Microfluidic Channels via Photoattachment Chemistry," *Anal. Chem.*, **76**, 1838-1843, 2004.
62. M. K. Chin and S. T. Ho, "Design and Modeling of Waveguide-Coupled Single-Mode Microring Resonators," *J. Lightwave Technol.*, **16**, 1433-1446, 1998.
63. D. R. Linde, *The CRC Handbook of Chemistry and Physics*, CRC Press, 2005.
64. J. P. Longtin and C.-H. Fan, "Precision laser-based concentration and refractive index measurement of liquid," *Microscale Thermophys. Eng.*, **2**, 261-272, 1998.
65. M. G. Raymer, Personal communication.
66. M. Sumetsky and Y. Dulashko, "Sensing an optical fiber surface by a microfiber with angstrom accuracy," *OFC*, ed., OTuL6-1 - OTuL6-3, 2006.
67. A. E. Siegman, *Lasers*, University Science Books, Sausalito, CA, 1986.
68. A. D. Fitt, K. Furusawa, T. M. Monro, and C. P. Please, "Modeling the Fabrication of Hollow Fibers: Capillary Drawing," *J. Lightwave Technol.*, **19**, 1924-1931, 2001.
69. S. C. Xue, R. I. Tanner, G. W. Barton, R. Lwin, M. C. J. Large, and L. Poladian, "Fabrication of microstructured optical fibers-part I: problem formulation and numerical modeling of transient draw process," *J. Lightwave Technol.*, **23**, 2245-2254, 2005.
70. S. C. Xue, R. I. Tanner, G. W. Barton, R. Lwin, M. C. J. Large, and L. Poladian, "Fabrication of Microstructured Optical Fibers—Part II: Numerical Modeling of Steady-State Draw Process," *J. Lightwave Technol.*, **23**, 2255-2266, 2005.
71. S. C. Xue, M. C. J. Large, G. W. Barton, R. I. Tanner, L. Poladian, and R. Lwin, "Role of Material Properties and Drawing Conditions in the Fabrication of Microstructured Optical Fibers," *J. Lightwave Technol.*, **24**, 853-860, 2006.
72. Y. Matsuura, R. Kasahara, T. Katagiri, and M. Miyagi, "Hollow infrared fibers fabricated by glass-drawing technique," *Optics Express*, **10**, 488-492, 2002.
73. G. J. Wegner, A. W. Wark, H. J. Lee, E. Codner, T. Saeki, S. Fang, and R. M. Corn, "Real-Time Surface Plasmon Resonance Imaging Measurements for the Multiplexed Determination of Protein Adsorption/Desorption Kinetics and Surface Enzymatic Reactions on Peptide Microarrays," *Anal. Chem.*, **76**, 5677-5684, 2004.
74. A.A.Ghoreyshi, F.A.Farhadpour, M.Soltanieh, and A. Bansal, "Transport of small polar molecules across nonporous polymeric membranes," *Journal of Membr. Sci.*, **211**, 193-214, 2003.
75. J. Scheuer and A. Yariv, "Optical annular resonators based on radial Bragg and photonic crystal reflectors," *Opt. Express*, **11**, 2003.
76. S. D. Hart, G. R. Maskaly, B. Temelkuran, P. H. Prideaux, J. D. Joannopoulos, and Y. Fink, "External Reflection from Omnidirectional Dielectric Mirror Fibers," *Science*, **296**, 510-513, 2002.

77. N. M. Litchinitser, A. K. Abeeluck, C. Headley, and B. J. Eggleton, "Antiresonant reflecting photonic crystal optical waveguides," *Opt. Lett.*, **27**, 1592-1594, 2002.
78. R. E. Harrington, "Flow birefringence of persistence length deoxyribonucleic acid. Hydrodynamic properties, optical anisotropy, and hydration shell anisotropy," *J. Am. Chem. Soc.*, **92**, 6957-6964, 1970.
79. T. Arakawa and Y. Kita, "Refractive Index of Proteins in Organic Solvents," *Anal. Biochem.*, **271**, 119-120, 1999.
80. M. A. Duguay, Y. Kokubun, T. L. Koch, and L. Pfeiffer, "Antiresonant reflecting optical waveguides in SiO₂-Si multilayer structures," *Appl. Phys. Lett.*, **49**, 13-15, 1986.
81. T. Baba, Y. Kokubun, T. Sakaki, and K. Iga, "Loss Reduction of an ARROW Waveguide in Shorter Wavelength and Its Stack Configuration," *J. Lightwave Technol.*, **6**, 1440 - 1445, 1988.
82. B. E. Little, J.-P. Laine, D. R. Lim, H. A. Haus, L. C. Kimerling, and S. T. Chu, "Pedestal antiresonant reflecting waveguides for robust coupling to microsphere resonators and for microphotonic circuits," *Opt. Lett.*, **25**, 73-75, 2000.
83. J.-P. Laine, B. E. Little, D. R. Lim, H. C. Tapalian, L. C. Kimerling, and H. A. Haus, "Microsphere Resonator Mode Characterization by Pedestal Anti-Resonant Reflecting Waveguide," *IEEE Photon. Technol. Lett.*, **12**, 1004-1006, 2000.
84. J. P. Laine, B. E. Little, D. R. Lim, H. C. Tapalian, L. C. Kimerling, and H. A. Haus, "Planar integrated wavelength-drop device based on pedestal antiresonant reflecting waveguides and high-Q silica microspheres," *Opt. Lett.*, **25**, 1636- 1638, 2000.
85. D. Erickson, X. Heng, Z. Li, T. Rockwood, T. Emery, Z. Zhang, A. Scherer, C. Yang, and D. Psaltis, "Optofluidics," *Optical Information Systems III*, Bahram Javidi and Demetri Psaltis, ed., Proc. SPIE **5908**, 59080S, 2005.
86. D. Psaltis, S. R. Quake, and C. Yang, "Developing optofluidic technology through the fusion of microfluidics and optics," *Nature Materials*, **442**, 381-386, 2006.
87. Q. Kou, I. Yesilyurt, and Y. Chen, "Collinear dual-color laser emission from a microfluidic dye laser," *Appl. Phys. Lett.*, **88**, 091101, 2006.
88. Z. Li, Z. Zhang, A. Scherer, and D. Psaltis, "Mechanically tunable optofluidic distributed feedback dye laser," *Opt. Express*, **14**, 10494-10499, 2006.